ACS APPLIED MATERIALS & INTERFACES

Research Article

Cite This: *ACS Appl. Mater. Interfaces* 2019, 11, 19017−19028

www.acsami.org

Magnetite-Coated Boron Nitride Nanosheets for the Removal of Arsenic(V) from Water

Raghubeer S. Bangari,[†] Arun K. Singh,[‡] Sadanandam Namsani,[‡] Jayant K. Singh,[‡] and Niraj Sinha*,[†]

[†]Department of Mechanical Engineering and [‡]Department of Chemical Engineering, Indian Institute of Technology Kanpur, Kanpur 208016, India

Supporting Information

ABSTRACT: It is widely known that the existence of arsenic (As) in water negatively affects humans and the environment. We report the synthesis, characterization, and application of boron nitride nanosheets (BNNSs) and Fe_3O_4-functionalized BNNS (BNNS−Fe_3O_4) nanocomposite for removal of As(V) ions from aqueous systems. The morphology, surface properties, and compositions of synthesized nanomaterials were examined using scanning electron microscopy, transmission electron microscopy, X-ray powder diffraction, surface area analysis, zero-point charge, and magnetic moment determination. The BNNS−Fe_3O_4 nanocomposites have a

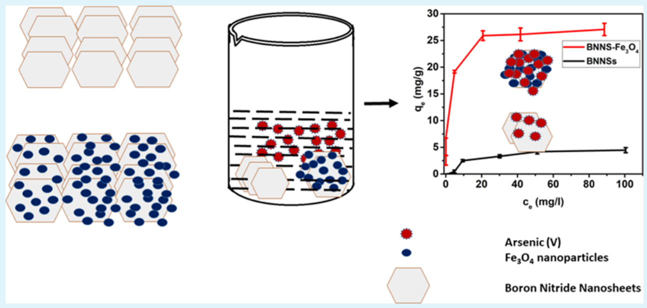

specific surface area of 119 m^2 g^{-1} and a high saturation magnetization of 49.19 emu g^{-1}. Due to this strong magnetic property at room temperature, BNNS−Fe_3O_4 can be easily separated in solution by applying an external magnetic field. From the activation energies, it was found that the adsorption of As(V) ions on BNNSs and BNNS−Fe_3O_4 was due to physical and chemical adsorption, respectively. The maximum adsorption capacity of BNNS−Fe_3O_4 nanocomposite for As(V) ions has been found to be 26.3 mg g^{-1}, which is 5 times higher than that of unmodified BNNSs (5.3 mg g^{-1}). This closely matches density functional theory simulations, where it is found that binding energies between BNNS−Fe_3O_4 nanocomposite and $As(OH)_5$ are 5 times higher than those between BNNSs and $As(OH)_5$, implying 5 times higher adsorption capacity of BNNS−Fe_3O_4 nanocomposite than unmodified BNNSs. More importantly, it was observed that the synthesized BNNS−Fe_3O_4 nanocomposite could reduce As(V) ion concentration from 856 ppb in a solution to below 10 ppb (>98.83% removal), which is the permissible limit according to World Health Organization recommendations. Finally, the synthesized adsorbent showed both separation and regeneration properties. These findings demonstrate the potential of BNNS−Fe_3O_4 nanocomposite for commercial application in separation of As(V) ions from potable and waste water streams.

KEYWORDS: *boron nitride nanosheets, Fe_3O_4 nanoparticles, adsorption, density functional theory, arsenic remediation*

1. INTRODUCTION

Although water covers majority of the surface of earth, only about 3% of water is clean. With increasing population, it is becoming a formidable task to meet the rising demand of clean water. Moreover, industrial development across the globe and anthropogenic activities such as mining, processing, and waste disposal have led to contamination of water (including groundwater) and soil with toxic heavy metals and organic compounds. Arsenic (As) is considered as one of the most hazardous heavy metals.[1] According to the literature, approximately 140 million population worldwide are exposed to drinking water with high As ions levels.[2] Long-term exposure to As ions may affect the central nervous system adversely, darken the skin, and may result in cancer of several types such as skin, lungs, liver, kidneys, and prostate.[3] Consequently, the limit of As ions in potable water has been set at 10 ppb by World Health Organization (WHO).[4] However, it has been reported through several studies that people in many states in India and neighboring Bangladesh are drinking water that has many times higher concentration of As ions than 10 ppb.[5−8] Therefore, there is an urgent need to control As ions levels in drinking water.

In the recent past, several technologies such as ion exchange, membrane filtration, chemical precipitation, and adsorption have been employed for removal of As ions from aquatic systems.[9] Among these techniques, efforts aimed at remediation of contaminants in water have focused primarily on adsorption (as a point-of-use treatment technology) due to advantages associated with them, such as simplicity of design, ease of operation, low cost, potential for regeneration, and sludge-free operation.[10,11] Several adsorption studies are reported for separation of As from water including a gamut of adsorbents such as metal oxides and activated carbons.[12−17] Compared to others, adsorbents derived by the incorporation of iron oxides such as magnetite (Fe_3O_4), hematite (α-Fe_2O_3), and magnetic maghemite (γ-Fe_2O_3) have been intensively

Received: December 23, 2018
Accepted: April 24, 2019
Published: April 24, 2019

DOI: 10.1021/acsami.8b22401
ACS Appl. Mater. Interfaces 2019, 11, 19017−19028

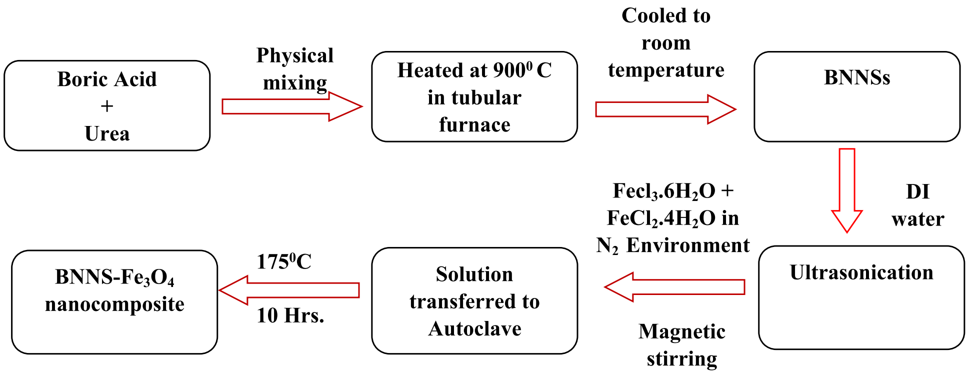

Figure 1. Schematic of the synthesis of BNNSs and BNNS−Fe_3O_4 nanocomposite.

investigated because of their nontoxicity, hydrophilicity, and better performance for As ion adsorption. Against this backdrop, various base substrates, including graphene oxide, activated carbons, mesoporous silica, and carbon nanotubes, have been used with the incorporation of iron oxide and investigated for separation of As and other ions from water as adsorbents.[9,18−22] Chandra et al. incorporated magnetite with reduced graphene oxide and were able to remove 99.9% of As(V) ions from aqueous stream.[18] Later, Tuna et al. modified the activated carbon with iron oxide and reported the maximum As(V) ion removal efficiency of 99.05%.[9] In the same year, Li et al. modified mesoporous silica by loading iron onto their surfaces. The maximum adsorption capacity of As(V) ions was reported as 26.25 mg g^{-1} by mobil composition of matter-41 (MCM-41) silica loaded with 10% of iron.[19] To study the adsorption of both As(III) ions and As(V) ions, Ntim and Mitra synthesized iron oxide−carbon nanotube hybrid and reported adsorption capacities as 1.723 mg g^{-1} for As(III) and 0.189 mg g^{-1} for As(V) ions.[20]

Good physical and chemical stability, high adsorption capacity, high surface area, nontoxicity, high recyclability, and easy separation from water solution are essential properties of adsorbents for their large-scale practical applications. Most of the reported nanocomposite adsorbents lack some of these aspects. Therefore, in this study, the feasibility of Fe_3O_4-loaded boron nitride nanosheets (BNNSs) for arsenic remediation in water to provide a novel, efficient, and economical adsorbent for As(V) ion removal is reported. Use of BNNSs for separation of As(V) ions from water is a promising approach because of their special properties such as polarity, high surface area, high thermal stability, high oxidation resistance, and inertness to most of the chemicals.[23,24] These unique properties make them an ideal supporter for several materials to adsorb/separate contaminants such as heavy metals from drinking water and waste water streams.[25] BNNSs were synthesized using bottom-up approach and functionalized with Fe_3O_4 nanoparticles to increase the number of adsorption sites for enhanced adsorption capacity. The adsorption capacities of BNNS−Fe_3O_4 nanocomposite and bare BNNSs have been determined and compared to density functional theory (DFT) simulations.

2. MATERIALS AND METHODS

2.1. DFT Simulations. DFT calculations have been employed to understand BNNS interactions with Fe_3O_4 and $As(OH)_5$ at the electronic level. To perform these calculations, boron nitride coronene $[(BN)_{12}H_{13}]$ has been used to corroborate our experimental results. The coronene boundary B and N atoms are saturated using hydrogen atoms. The geometry optimizations and the binding-energy calculations have been carried out by a hybrid exchange correlation functional (CAM-B3LYP) using 6-31G(d,p) basis set. The hybrid qualities of B3LYP are combined with long-range correction by CAM-B3LYP.[26] Polarization continuum model with SCRF methods implemented in Gaussian09 has been used to account the effect of solvent on binding mechanism and binding energy (BE). BEs of $As(OH)_5$ on both BNNSs and BNNS−Fe_3O_4 composites have been computed and compared. The BE of $As(OH)_5$ on the BNNS−Fe_3O_4 composite is computed using the following relation

$$\mathrm{BE} = E(\mathrm{BNNS} - \mathrm{Fe_3O_4} + \mathrm{As(OH)_5}) - [E(\mathrm{BNNS} - \mathrm{Fe_3O_4}) + E(\mathrm{As(OH)_5})]$$

In the case of BNNSs, the binding energy is computed using the following relation

$$\mathrm{BE} = E(\mathrm{BNNSs} + \mathrm{As(OH)_5}) - [E(\mathrm{BNNSs}) + E(\mathrm{As(OH)_5})]$$

2.2. Experiments. *2.2.1. Materials.* Urea (≥99.0% purity) and boric acid (≥99.5% purity) were obtained from HiMedia and Sigma-Aldrich, respectively. Iron(II) chloride tetrahydrate (≥98.0% purity) and ferric chloride hexahydrate (≥98.0% purity) were purchased from Alfa Aesar and SD Fine-Chem Limited, India, respectively. Sodium hydroxide pellets (≥97% purity) were acquired from Finar Limited, India. Hydrochloric acid (37%) was acquired from Fisher Scientific, India. Sodium arsenate dibasic heptahydrate (≥98.5% purity) and standard solution of As ions used in experiments were procured from Loba Chemie, India. Unless otherwise stated, all of the chemicals mentioned above were used as received. Sodium arsenate dibasic heptahydrate was selected as a source of As(V) ions. All of the solutions were prepared by ultrapure deionized (DI) water (18.2 MΩ cm), which was obtained from a Millipore Milli-Q water purification system.

2.2.2. Synthesis of BNNSs. Boric acid and urea were used as precursors to synthesize BNNSs. Both the precursors, at a fixed molar ratio of 1:48, were physically mixed in a mortar and pestle. The mixture was then transferred to a tubular furnace in a quartz boat and heated up to 900 °C at a heating rate of 4 °C min^{-1}. The mixture was retained at this temperature for 5 h under nitrogen environment.[27] After the completion of chemical reaction, the tubular furnace was cooled to room temperature gradually. White BNNSs were obtained upon cooling.

2.2.3. Synthesis of BNNS−Fe_3O_4 Nanocomposite. In 100 mL of DI water, 150 mg of BNNS was added. This was followed by 30 min of ultrasonication (Oscar, India). In a fixed molar ratio (2:1), $FeCl_3\cdot 6H_2O$ and $FeCl_2\cdot 4H_2O$ were subsequently added into the solution. The solution was subjected to magnetic stirring for 3.5 h. During the reaction, 3 mL of NH_4OH was added dropwise through a syringe to adjust the solution pH to 8.0 that is necessary for the synthesis of magnetic nanoparticles (Fe_3O_4).[28] Nitrogen gas environment was maintained throughout the reaction. At the end of the reaction, 50 mL of the solution was transferred to an autoclave having a 100 mL Teflon vial. The autoclave was perfectly closed, heated to 175 °C for

DOI: 10.1021/acsami.8b22401
ACS Appl. Mater. Interfaces 2019, 11, 19017−19028

10 h, and then cooled down to room temperature gradually. After washing with DI water, the product was dried at 65 °C. The dried product was heated again to 300 °C for 2 h in a muffle furnace to enhance the binding of Fe_3O_4 nanoparticles, as reported by Chen et al.[29] The schematic of the synthesis of BNNSs and BNNS−Fe_3O_4 nanocomposites is shown in Figure 1.

2.2.4. Characterization and Measurements. The morphologies of synthesized BNNSs and BNNS−Fe_3O_4 nanocomposite were characterized by field emission scanning electron microscopy (FESEM, Carl Zeiss) and high-resolution transmission electron microscopy (HR-TEM, FEI Titan G2 60−300 microscope). Nitrogen gas sorption isotherms were measured at −196 °C on a surface area analyzer and a porosity analyzer (Quantachrome Autosorb iQ). All samples were degassed at 180 °C in vacuum for 10 h prior to isotherm measurement. The Brunauer−Emmett−Teller (BET) method was employed to calculate the specific surface area (SBET), while the Barrett−Joyner−Halenda method was used to calculate the pore size distribution (PSD). Fourier transform infrared (FTIR) spectroscopy was used to analyze the composition of synthesized materials using PerkinElmer Spectrum Two spectrometer. FTIR absorption spectra were recorded in the 4000−400 cm^{-1} frequency range with a spectral resolution of 2 cm^{-1}. KBr (200 mg) was mixed with 2.0 mg of each test sample in an agate mortar and pressed into pellets of 13 mm diameter. X-ray diffractometry (XRD, Panalytical X'Pert Powder) was used to analyze the crystalline nature of BNNSs and BNNS−Fe_3O_4 nanocomposite. The patterns were collected by using Cu Kα radiation (λ = 1.506 Å) from 10 to 70° at a sweep rate of 2° min^{-1}. The accelerating voltage and current were 45 kV and 40 mA, respectively. The point of zero charge (pH_{pzc}) was determined by pH drift method.[30] With the help of a vibrating sample magnetometer (EV7 ADE-DMS), the magnetic properties of the nanocomposites were obtained at room temperature. Inductively coupled plasma mass spectroscopy (Agilent 7900, ICP-MS) was used to measure the concentration of As(V) ions.

2.2.5. Arsenic(V) Adsorption and Effect of Process Variables. Batch experiments were performed to investigate how significant process variables (initial pH, temperature, and dose) affect the adsorption behavior of As(V) ions on BNNSs and BNNS−Fe_3O_4 nanocomposite. For sorption studies, known amounts of adsorbents (BNNSs and BNNS−Fe_3O_4 nanocomposite) were dispersed in 25 mL of As(V) ion solution in polypropylene (Tarsons) centrifuge tubes at different initial pH values and temperatures. In the initial study, the pH of the As(V) ion solution was in the range of 2−10 and was adjusted precisely by using 0.1 M HCl and 0.1 M NaOH. From the initial pH study, the highest adsorption was found at pH 2. Therefore, subsequent experiments were conducted at this pH. The sorption experiments were performed in a thermo-controlled orbital shaker (Mahendra Scientific, India) for 10 h at 180 rpm at different temperatures (10, 17, 25, 30, 35, and 40 °C). The equilibrated samples were taken out, and adsorbent was separated with a 0.22 μm syringe filter (Millex). The residual concentration of As(V) ions in the solution was determined using ICP-MS. The equilibrium uptake (q_e in mg g^{-1}) was calculated by using the following equation

$$q_e = \frac{(C_0 - C_e)V}{m} \tag{1}$$

where C_0 (mg L^{-1}) is the initial concentration of As(V) ions, C_e (mg L^{-1}) is the equilibrium concentration of As(V) ions, V (L) is the volume of solution, and m (g) is the mass of adsorbent. All of the adsorption experiments reported in this study were performed in triplicate.

2.2.5.1. Kinetic Studies. To conduct the adsorption kinetics study, 0.4 g of adsorbent per liter was used in an As(V) ion solution (25 mL, 50 mg L^{-1}) at pH 2. Adsorption kinetics of As(V) ions uptake by BNNSs and BNNS−Fe_3O_4 were determined by fitting the obtained experimental data to pseudo-first-order (PFO) and pseudo-second-order (PSO) kinetic models, which are expressed, respectively, as

$$\ln(q_e - q_t) = \ln q_e - k_1 t \tag{2}$$

$$\frac{t}{q_t} = \frac{1}{k_2 q_e^2} + \frac{t}{q_e} \tag{3}$$

In eqs 2 and 3, q_t denotes the amount of adsorbed solute at time t, k_1 (min^{-1}) represents PFO rate constant, and k_2 signifies PSO kinetic rate constant (g mg^{-1} min^{-1}).

2.2.5.2. Adsorption Isotherm Study. The initial concentration of As(V) ions was varied to perform the adsorption isotherm study. In the prepared solutions, 0.4 g of adsorbents per liter were dispersed. The pH was maintained at 2.0. The samples were placed in a shaker for 10 h at 180 rpm. Langmuir and Freundlich isotherm models were employed for analyzing the isotherm data. The Langmuir isotherm is expressed as

$$q_e = \frac{q_m C_e K_L}{1 + C_e K_L} \tag{4}$$

where K_L (mL mg^{-1}) denotes the Langmuir adsorption equilibrium constant and q_m (mg g^{-1}) represents the maximum adsorption capacity of the adsorbent. The Freundlich isotherm is expressed as follows

$$q_e = K_F C_e^{1/n} \tag{5}$$

where K_F and n are constants that measure the adsorption capacity and intensity, respectively.[31]

3. RESULTS AND DISCUSSION

3.1. Adsorption of As(V) Ions on BNNS−Fe_3O_4 Nanocomposite (DFT). To quantify the interaction strength of BNNSs and BNNS−Fe_3O_4 nanocomposite with $As(OH)_5$, the geometries were optimized at the B3LYP/6-31G(d,p) level of theory.[32] Full geometry optimizations for the considered BN−Fe_3O_4 system have been performed with various spin states S = 1, 3, and 5. Triplet state is found to have the lowest energy compared to S = 1 and S = 5 states. However, the BEs calculated for $As(OH)_5$ and BNNS−Fe_3O_4 system with S = 3 and 5 state energies are positive in magnitude (166.729 and 54.55 kJ mol^{-1}, respectively). In contrast, the BE calculated using S = 1 is −200.381 kJ mol^{-1}. Hence, S = 1 state is the most stable configuration, which is used for further analysis. The optimized geometries of BNNSs and $As(OH)_5$ are shown in Figure 2a,b, respectively. Further, Figure 2c shows the top view of the BNNS−Fe_3O_4 nanocomposite optimized geometry, while its side view is shown in Figure 2d. From these figures, the formation of BNNS−Fe_3O_4 nanocomposite through the B−O and N−Fe bond formation can be clearly seen. The average distance between the Fe_3O_4 and BNNS surface is 2.5 Å. Further, geometry optimizations of BNNS−$As(OH)_5$ and BNNS−Fe_3O_4−$As(OH)_5$ structures have been performed using DFT calculations and the BEs have been evaluated using the procedure mentioned in Section 2.1. Figure 3a,b shows the optimized structures of BNNS−$As(OH)_5$ and BNNS−Fe_3O_4−$As(OH)_5$ systems, respectively, which have been obtained using DFT. The computed BEs from DFT calculations for $As(OH)_5$ with BNNSs and BNNS−Fe_3O_4 composites are −43.100 and −200.381 kJ mol^{-1}, respectively. The $As(OH)_5$ binding energy with BNNS−Fe_3O_4 is 4.65 times higher than that with unmodified BNNSs. This clearly demonstrates the possibility of achieving high adsorption capacity for BNNS−Fe_3O_4 compared to the unmodified BNNSs.

3.2. Characterization of BNNSs and BNNS−Fe_3O_4. The as-prepared BNNSs and BNNSs−Fe_3O_4 were characterized by a variety of methods to determine the surface morphology, compositions, and surface properties. Figure 4a shows the

DOI: 10.1021/acsami.8b22401
ACS Appl. Mater. Interfaces 2019, 11, 19017−19028

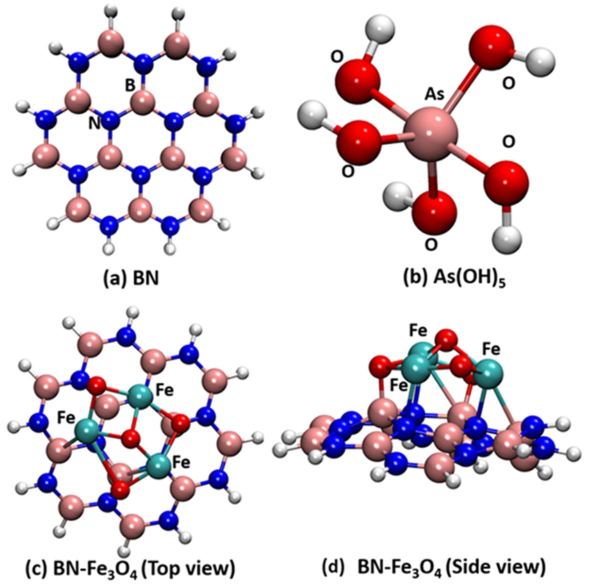

Figure 2. Optimized geometries of (a) BNNSs, (b) As ions $(OH)_5$, (c) BNNS−Fe_3O_4 structure top view, and (d) BNNS−Fe_3O_4 structure side view.

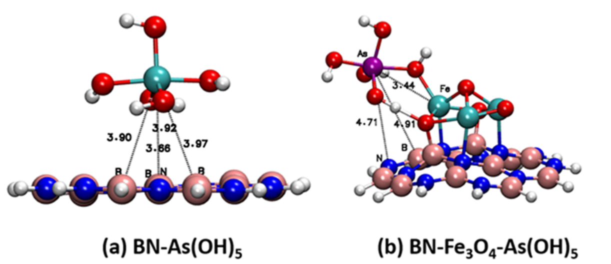

Figure 3. Structures obtained from DFT optimization: (a) BNNSs−As ion $(OH)_5$ and (b) BNNS−Fe_3O_4−As ion $(OH)_5$ nanocomposites.

HRTEM image of BNNSs, in which lattice fringes can be seen clearly (inset of Figure 4a). Figure 4b shows the selected area electron diffraction (SAED) pattern of BNNSs. The ring patterns indicate their amorphous nature. The inner ring and the outer ring represent (002) and (101) planes, respectively. The diameter of the BNNS−Fe_3O_4 nanocomposite was found to be 10−22 nm, as shown in Figure 4e. The SAED pattern of the BNNS−Fe_3O_4 nanocomposite shows its polycrystalline nature (see Figure 4f). The indexed rings represent the diffraction corresponding to Fe_3O_4, which confirms the formation of BNNS−Fe_3O_4 nanocomposite. The HRTEM images in Figure 4c show lattice fringes of BNNS−Fe_3O_4 nanocomposite. The lattice spacing was found to be 0.27 nm, as shown in Figure 4i. High-angle annular dark-field (HAADF) imaging and elemental mapping of BNNSs and BNNSs−Fe_3O_4 nanocomposite give the distribution of boron, nitrogen, iron, and oxygen, as shown in Figure 4c,d and g,h, respectively. The figure reveals the uniform distribution of elements present in the adsorbents. FESEM image in Figure S1a clearly shows sheet morphology of BNNSs, while Figure S1b shows the deposition of Fe_3O_4 nanoparticles on BNNSs.

The nitrogen (N_2) adsorption−desorption isotherm and PSD were plotted for BNNSs and BNNS−Fe_3O_4 nanocomposite samples (see Figure S2). PSD clearly indicates the presence of micro- (pore size less than 2 nm) and meso- (pore size 2−50 nm) pores in the BNNSs, as shown in Figure S2b. Therefore, BNNSs showed the presence of hierarchical porosity. SBET was calculated to be ∼1599.1 $m^2\ g^{-1}$, while the average pore diameter and total pore volume were determined to be 1.43 nm and 1.212 cc g^{-1}, respectively. As shown in Figure S2d, PSD also confirms the hierarchical porosity of the BNNS−Fe_3O_4 nanocomposite. The SBET was 119.1 $m^2\ g^{-1}$. The average pore diameter and total pore volume were determined to be 17.41 nm and 0.355 cc g^{-1}, respectively. It is assumed that the growth of Fe_3O_4 nanoparticles on pristine BNNSs surface blocked the pores of BNNSs, which resulted in the low surface area of nanocomposite. This is confirmed by the PSD and low pore volume of the nanocomposite.

The structural information about the pristine BNNSs and BNNS−Fe_3O_4 nanocomposite was obtained by XRD. All of the peaks were labeled for BNNSs and BNNS−Fe_3O_4. As shown in Figure S3a, diffraction peaks of BNNSs were at 24.17 and 42.55°.[24,33] They represent (002), (100), and (101) planes of hexagonal BNNSs, respectively. Diffraction peaks of the BNNS−Fe_3O_4 nanocomposite were at around 30.37, 35.65, 43.53, 53.85, 57.37, and 63.07°.[34−36] As shown in Figure S3b, all of the peaks relate to (220), (311), (400), (422), (511), and (440) planes, respectively. This matches with JCPDS card no. 19-0629. Besides, all of the indexed planes directly matched with the SAED pattern of BNNS−Fe_3O_4 nanocomposite. The nature of chemical bonds of the synthesized adsorbents was determined using FTIR analysis. In Figure 5a, the vibration peak at around 790 cm^{-1} indicates the out-of-plane bending vibrations of B−N bonds in BNNSs. Further, the vibration peak at around 1380 cm^{-1} indicates the in-plane vibration of B−N bonds. In Figure 5b, the band in the range of 558−636 cm^{-1} depicts symmetric stretching of Fe−O bond vibration.[37] Further, stretching vibration of Fe−O−Fe and structural vibration of Fe−OH are designated by peaks at 857 and 1030 cm^{-1}, respectively.[38,39] Another peak at 1400 cm^{-1} shows in-plane vibration of sp^2-bonded B−N bonds, while the peak at 1627 cm^{-1} shows bending vibration of H_2O adsorbed on the surface of nanocomposite.[28] The peaks 2852 and 2925 cm^{-1} correspond to $-BNH_2$ group.[40] Finally, the broad band at 3415 cm^{-1} is attributed to B−OH group.[41]

Saturation magnetization (Ms) is a pivotal factor for evaluating the magnetic separation ability of an adsorbent. With a conventional magnet, M_S of 18 emu g^{-1} has been described sufficient for this purpose.[42] The M_S of BNNS−Fe_3O_4 nanocomposite was found to be 49.19 emu g^{-1} (see Figure 5c), which corresponded to a magnetic moment of 2.04 μ_B. The value of M_S of the synthesized sample implies successful loading of a large amount of Fe_3O_4 on BNNS surface, and therefore, highly magnetic nature of the BNNS−Fe_3O_4 nanocomposite. Thus, the Ms value achieved for the BNNS−Fe_3O_4 nanocomposite was sufficient for easy separation by using a handy magnet, as can be seen in Figure 5d.

3.3. Effects of the Adsorption Parameters. *3.3.1. Effect of pH.* According to previous studies, the surface charge of the adsorbent varies with the pH of the solution.[11,38] Therefore, it is essential to study how the adsorption capacity of the adsorbents is affected by pH. During the pH change from 2 to 12, the As(V) ions dissociate into $H_2AsO_4^-$, $HAsO_4^{2-}$, and AsO_4^{3-} according to the dissociation constants pK_{a1} = 2.1, pK_{a2} = 6.7, and pK_{a3} = 11.2, respectively.[43] Therefore, experiments were performed to study the effect of pH on adsorption of As(V) ions for both the adsorbents in the range of 2−10. The

DOI: 10.1021/acsami.8b22401
ACS Appl. Mater. Interfaces 2019, 11, 19017−19028

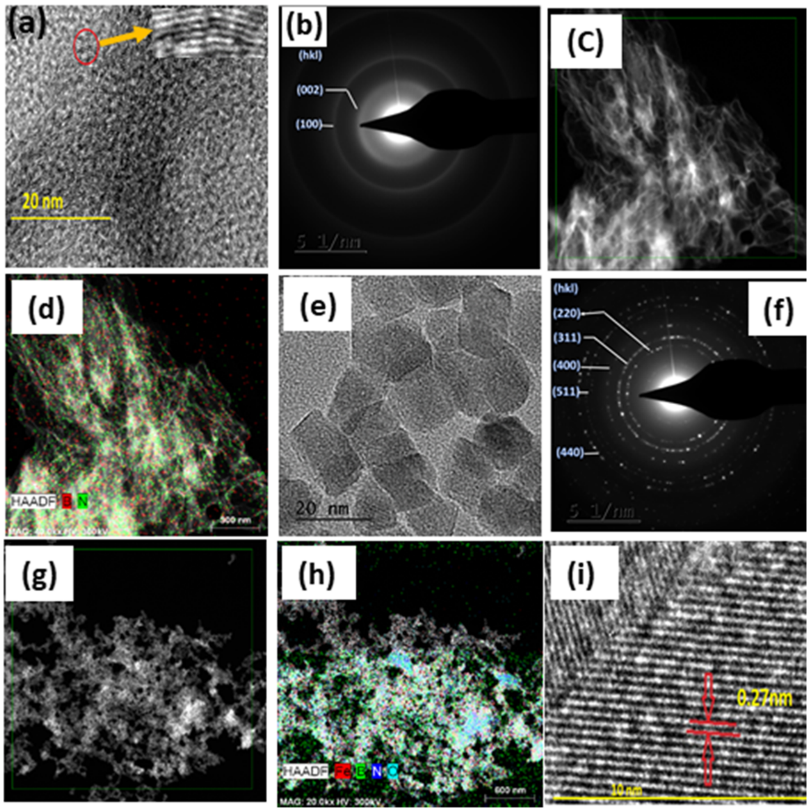

Figure 4. (a) HRTEM image of BNNSs (inset: fringes of BN), (b) SAED patterns of BNNSs, (c) HAADF images of BNNSs, (d) elemental distribution of BNNSs, (e) HRTEM image of BNNS−Fe_3O_4 nanocomposite, (f) SAED pattern of BNNS−Fe_3O_4 nanocomposite, (g) HAADF image of BNNS−Fe_3O_4 nanocomposite, (h) elemental distribution of BNNS−Fe_3O_4 nanocomposite, and (i) lattice spacing of nanocomposite.

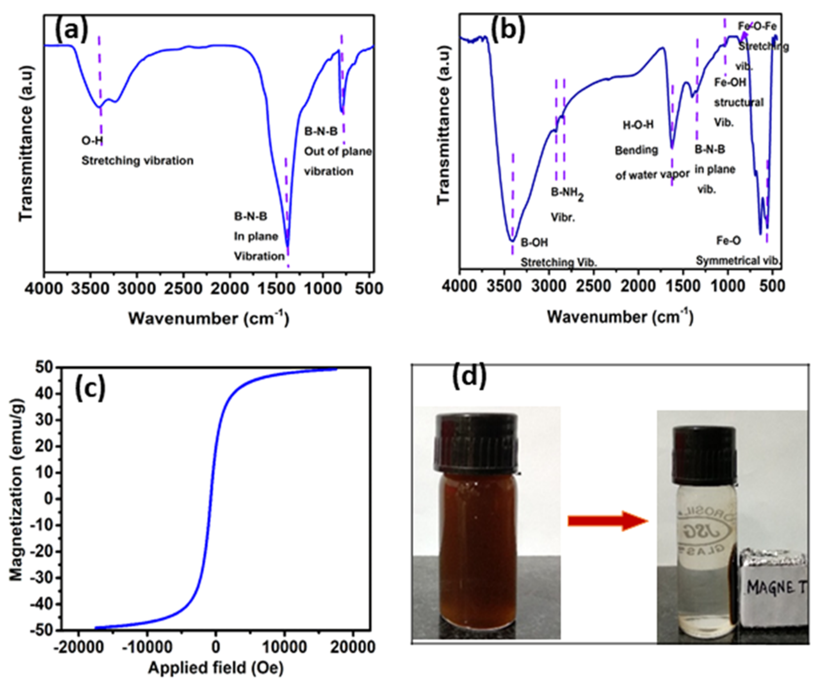

Figure 5. FTIR spectra of (a) BNNSs and (b) BNNS−Fe_3O_4 nanocomposite, (c) M−H curve of BNNS−Fe_3O_4 nanocomposite, and (d) magnetic separation of BNNS−Fe_3O_4 nanocomposite by a magnet.

adsorption of As(V) ions depicted pH dependency. As can be deduced from Figure 6a, the maximum adsorption of As(V) ions for both BNNSs and BNNS−Fe_3O_4 nanocomposite occurred under acidic conditions (pH 2) and decreased with increase in pH. The point of zero charge (pH_{pzc}) values of BNNS−Fe_3O_4 and BNNSs were 2.86 and 8.78, respectively. When pH < pH_{pzc}, the BNNS−Fe_3O_4 nanocomposite surface is positively charged because of protonation reaction. There-

DOI: 10.1021/acsami.8b22401
ACS Appl. Mater. Interfaces 2019, 11, 19017−19028

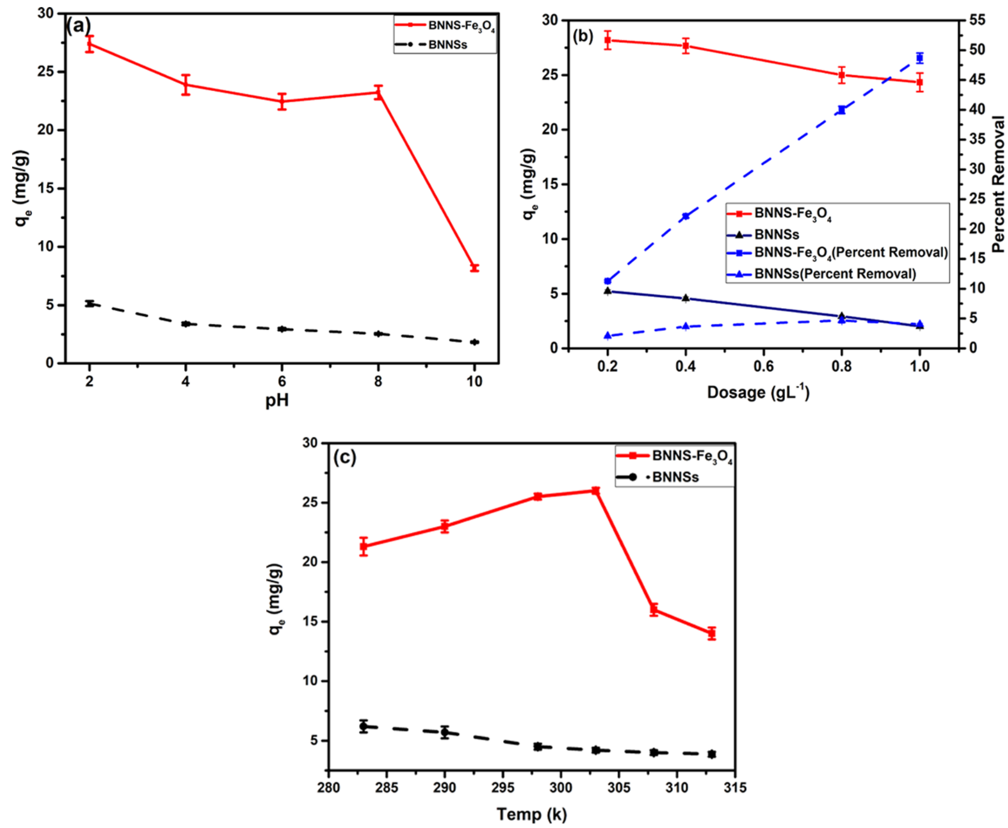

Figure 6. Effect of (a) pH, (b) adsorbent dose, and (c) temperature on As(V) ion removal by BNNSs and BNNS−Fe_3O_4 nanocomposite.

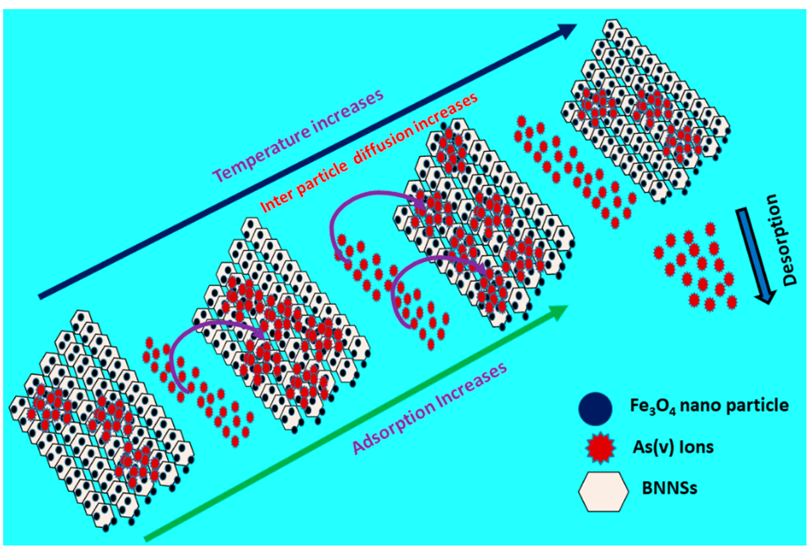

Figure 7. Schematic of the effect of temperature and adsorption kinetics of interparticle diffusion of As(V) ions on BNNS−Fe_3O_4 nanocomposite (interparticle mechanism).

fore, strong electrostatic attraction takes place between BNNS−Fe_3O_4 nanocomposite and negatively charged species of As(V) ions, leading to high adsorption of As(V) ions. Subsequently, at pH > pH_{pzc}, the surface charge of nanocomposite is negative due to adsorption of OH^{-1} ions. Stepwise increase in pH enhanced the electrostatic repulsion between BNNSs−Fe_3O_4 nanocomposite and oxyanion of As(V) ions. This resulted in reduction in the adsorption capacity of nanocomposite. Similar results have been communicated by other researchers.[18,44,45]

3.3.2. Effect of Adsorbent Dose. Figure 6b shows the effect of adsorbent (BNNSs and BNNS−Fe_3O_4) dose on the adsorption capacity of As(V) ions. The dose of adsorbents was increased from 0.2 to 1.0 g of adsorbent per liter, and the initial concentration of As(V) ions was maintained at 50 mg L^{-1} at pH 2. From the figure, one can see that the percent removal increases with dosage while the adsorption capacity decreases with dosage for both the adsorbents. The increase in percent removal is higher in BNNS−Fe_3O_4 (~48.7%) than in BNNSs (~4%) at 1.0 g of adsorbent per liter, due to increase

DOI: 10.1021/acsami.8b22401
ACS Appl. Mater. Interfaces 2019, 11, 19017−19028

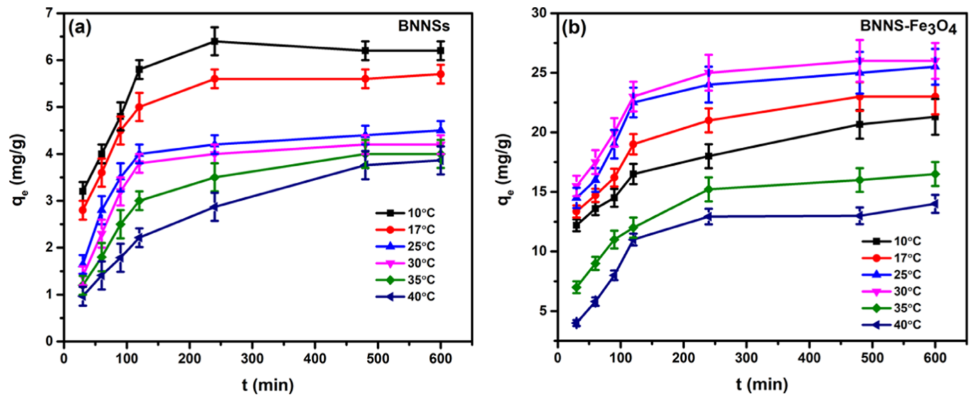

Figure 8. Effects of contact time and temperature on the adsorption of As(V) ions onto (a) BNNSs and (b) BNNS−Fe_3O_4 nanocomposite.

Table 1. Pseudo-First-Order and Pseudo-Second-Order Kinetic Model Rate Constants for As(V) Ion Adsorption on BNNSs and BNNS−Fe_3O_4 Nanocomposite (Experimental Conditions: Initial As(V) Ion Concentration, 50 mg L^{-1}; pH, 2.0; and Dose of Adsorbent, 0.4 g L^{-1})

pseudo-first-order kinetic model (PFO)								
	BNNSs				BNNS−Fe_3O_4			
T (K)	q_{exp} (mg g^{-1})	q_{cal} (mg g^{-1})	K_1 (min $^{-1}$)	R^2	q_{exp} (mg g^{-1})	q_{cal} (mg g^{-1})	K_1 (min $^{-1}$)	R^2
283	6.20 ± 0.5	2.280	0.0074	0.813	21.301 ± 0.75	11.001	0.0058	0.987
290	5.70 ± 0.5	2.289	0.0078	0.782	23.00 ± 0.5	12.379	0.0078	0.967
298	4.50 ± 0.25	2.901	0.0104	0.871	25.50 ± 0.25	14.614	0.0100	0.929
303	4.20 ± 0.25	3.334	0.0127	0.896	26.00 ± 0.25	17.690	0.0137	0.933
308	4.00 ± 0.2	3.310	0.0083	0.963	16.50 ± 0.5	10.044	0.0067	0.957
313	3.86 ± 0.2	4.063	0.0074	0.978	14.00 ± 0.5	14.296	0.0111	0.974
pseudo-second-order kinetic model (PSO)								
	BNNSs				BNNS−Fe_3O_4			
T (K)	q_{exp} (mg g^{-1})	q_{cal} (mg g^{-1})	K_2 (g mg^{-1} min $^{-1}$)	R^2	q_{exp} (mg g^{-1})	q_{cal} (mg g^{-1})	K_2 (g mg^{-1} min $^{-1}$)	R^2
283	6.20 ± 0.5	6.578	0.0057	0.997	21.301 ± 0.75	22.523	0.0010	0.997
290	5.70 ± 0.5	6.000	0.0054	0.998	23.00 ± 0.5	24.449	0.0011	0.999
298	4.50 ± 0.25	4.807	0.0052	0.997	25.50 ± 0.25	26.809	0.0011	0.999
303	4.20 ± 0.25	4.595	0.0046	0.995	26.00 ± 0.25	27.322	0.0013	0.999
308	4.00 ± 0.2	4.589	0.0027	0.997	16.50 ± 0.5	18.181	0.0010	0.991
313	3.86 ± 0.2	4.761	0.0015	0.996	14.00 ± 0.5	15.748	0.0007	0.999

in the number of active sites. At the same time, dose might increase the aggregation of BNNSs in water due to strong van der Waals interaction between BN layers, resulting in reduction of adsorption capacity.[46,47] The maximum adsorption capacity for both the adsorbents was found at 0.2 g L^{-1} of adsorbent.

3.3.3. Effect of Temperature. The experiments were carried out at 10, 17, 25, 30, 35, and 40 °C to analyze the influence of temperature on adsorption (see Figure 6c). With an increase in temperature, different behaviors were shown by the two adsorbents. As the temperature increased, the adsorption capacity of BNNSs decreased, which is evident from Figure 6c. It shows the exothermic behavior of BNNSs. In contrast, the adsorption capacity of BNNS−Fe_3O_4 initially increased and then decreased with increase in temperature (see Figure 6c). Therefore, we interpret that the adsorption was endothermic initially and became exothermic beyond 30 °C. This is consistent with the previously reported studies.[48] The optimum adsorption capacity was found to be at 30 °C.

Further, the exothermic nature of BNNSs is due to the physisorption (as will be shown in Section 3.3.6). Here, the bonding between the adsorbent and adsorbate is mainly due to weak van der Waal forces. Therefore, the weak forces decrease with an increase in the temperature. In the case of BNNS−Fe_3O_4, the adsorption is influenced by chemical adsorption. It has been reported in the literature that the chemisorption first increases since more number of adsorbate ions acquire sufficient energy to undergo chemisorption, which is provided by an increase in temperature.[49,50] Further increase in temperature leads to breaking of bonds between adsorbate and adsorbent, resulting in decrease in adsorption capacity. This has been explained schematically in Figure 7. Moreover, we have used kinetic models to analyze the typical behavior of BNNS−Fe_3O_4 with temperature. To this end, we have applied kinetic model given by Boyd et al.[51] to examine the actual rate-controlling step taking part in adsorption reaction (see Figure 8). From the analysis, it has been found that adsorption is governed by external mass transport (or film diffusion). Therefore, as the temperature increases, the external mass transport increases. This may increase the adsorption capacity up to optimum temperature. Further rise in temperature reduces the adsorption capacity due to increase in the solubility of the adsorbate.[52] Therefore, the adsorption capacity decreases. Similar observations are reported by Pokhrel et al. and Mondal et al.[16,53] Pokhrel et al. reported that the removal capacity of As(V) ions increased when the

DOI: 10.1021/acsami.8b22401
ACS Appl. Mater. Interfaces 2019, 11, 19017−19028

temperature was increased from 5 to 30 °C. A decreasing trend between 30 and 60 °C was observed by Mondal et al. In contrast, the adsorption capacity of BNNSs was found to decrease as the temperature increased. This can be explained as follows. Brownian motion increases with an increase in temperature, thereby breaking the intermolecular hydrogen bonding. Therefore, decrease in adsorption capacity is observed.[54]

3.3.4. Adsorption Kinetics. The adsorption kinetics of As(V) ion removal was determined to understand the adsorption behavior of BNNSs and BNNSs−Fe_3O_4 nanocomposite. The effects of contact time and temperature on the adsorption of As(V) ions by both the adsorbents are shown in Figure 8a,b, respectively. According to the results, the adsorption capacity increased rapidly up to 120 min, increased gradually thereafter, and achieved equilibrium in 10 h. Both the adsorbents followed the same trend. Experimental data were fitted to PFO and PSO kinetic models. The kinetics parameters obtained from the two models are presented in Table 1. The correlation coefficient (R^2 = 0.99) indicated that this adsorption process followed the PSO model and the adsorption took place through the chemical interaction.[20,21] The calculated and experimental adsorption capacities were found to be in line.

3.3.5. Adsorption Isotherms. Adsorption isotherm models can be used to describe the distribution of adsorbed molecules on the adsorbents after reaching the equilibrium state. Langmuir and Freundlich isotherm models, as described in Section 2.2.5.2, have been used in this study. Langmuir isotherm assumes ideal monolayer formation due to homogeneous adsorbent surface. Conversely, Freundlich isotherm assumes multilayer adsorption on the heterogeneous adsorbent surface. The adsorption isotherm of BNNSs and BNNS−Fe_3O_4 nanocomposite is shown in Figure 9. It was found that

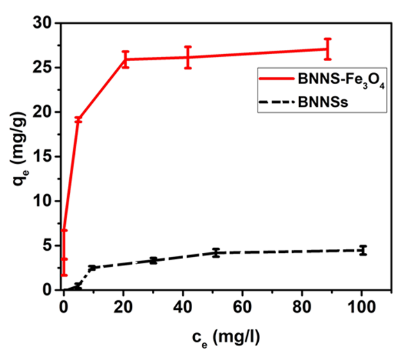

Figure 9. Adsorption isotherm of BNNSs and BNNS−Fe_3O_4 nanocomposite.

the Langmuir model has high correlation coefficient (R^2 > 0.999) than the Freundlich model (R^2 > 0.908). Consequently, it was inferred that there was a monolayer adsorption of As(V) ions on the homogeneous surface of BNNS−Fe_3O_4 nanocomposite. The adsorption capacities of BNNSs and BNNS−Fe_3O_4 nanocomposite were 5.3 and 26.3 mg g^{-1}, respectively, at room temperature (298 K). This 5-fold increase is broadly in agreement with the theoretical simulations carried out using DFT. The adsorption constant determined from the isotherm models are presented in Table 2. The values of the Freundlich constant (n = 2.03 and 3.76) for both the adsorbents imply that the adsorption of As(V) ions is favored on both of them.[18]

Table 2. Langmuir and Freundlich Adsorption Isotherm Parameters for BNNSs and BNNS−Fe_3O_4 Nanocomposite (Experimental Conditions: Initial Concentration of As(V) Ions, 50 mg L^{-1}; Temperature, 25 °C; pH, 2.0; and Dose of Adsorbent, 0.4 g L^{-1})

isotherm models	isotherm parameters	BNNSs	BNNS−Fe_3O_4
Langmuir	Q_{max} (mg g^{-1})	5.305	26.315
	K_L (L mg^{-1})	0.058	1.938
	R^2	0.981	0.999
Freundlich	k_F (mg^{1-n} L^n g^{-1})	0.561	10.138
	n	2.030	3.763
	R^2	0.822	0.908

3.3.6. Adsorption Activation Energy. The activation energies (E_a in kJ mol^{-1}) of adsorption on BNNSs and BNNS−Fe_3O_4 were calculated by the Arrhenius equation expressed as

$$\ln k = \ln A - \frac{E_a}{RT} \tag{6}$$

where k is the rate constant, A is the Arrhenius constant (g mg^{-1} min^{-1}) that is a temperature-independent factor, R is the gas constant (8.314 J mol^{-1}), and T is the temperature (K). Using the PSO rate constant, the plot of $\ln k$ versus the reciprocal of T resulted in straight lines for both the adsorbents (see Figure 10). From the slope, the activation energies of BNNSs and BNNS−Fe_3O_4 nanocomposite were calculated as −4.46 and −41.95 kJ mol^{-1}, respectively. The negative activation energy values indicate that the adsorption process was exothermic in nature. Moreover, the adsorption capacity decreases with an increase in temperature because of increased solubility of the adsorbate species.[52] Typically, the magnitude of activation energy is directly related to physical and chemical adsorption.[55] Since the reactions are readily reversible and equilibrium is attained quickly, the energy requirements for physical adsorption are small (5−40 kJ mol^{-1}). Chemical adsorption requires relatively higher energies (40−800 kJ mol^{-1}) due to involvement of stronger forces. On the basis of magnitude of activation energy, one can conclude that the adsorption of As(V) ions on BNNSs was dominated by physical adsorption. Conversely, adsorption in the case of BNNSs−Fe_3O_4 nanocomposite was influenced by chemical adsorption.

3.4. Application of BNNS−Fe_3O_4 Nanocomposite for Higher As(V) Ion Concentrations and Its Comparison with Other Adsorbents. Surface water from large rivers and dams is normally used for municipal supply in developing countries.[56] According to the literature, the surface water and shallow groundwater under aerobic conditions are mainly contaminated with As(V) since it is dominant under oxidizing conditions. Therefore, the synthesized adsorbent was tested to find the maximum concentration of these ions that could be brought to below 10 ppb.[57−60] With optimum experimental parameters, the BNNS−Fe_3O_4 nanocomposite has the potential to reduce As(V) ions in contaminated water from 856 ppb to below 10 ppb (see Table 3). The BNNS−Fe_3O_4 nanocomposite showed high adsorption capacity at pH 2 because of electrostatic attraction and surface complexation. At 2.1 < pH < 6.7, As(V) ions exist as $H_2AsO_4^-$. At pH 2, there is a strong electrostatic force between the BNNSs−Fe_3O_4 nanocomposite and negatively charged arsenate ions present on the surface. This leads to high adsorption capacity at low

DOI: 10.1021/acsami.8b22401
ACS Appl. Mater. Interfaces 2019, 11, 19017−19028

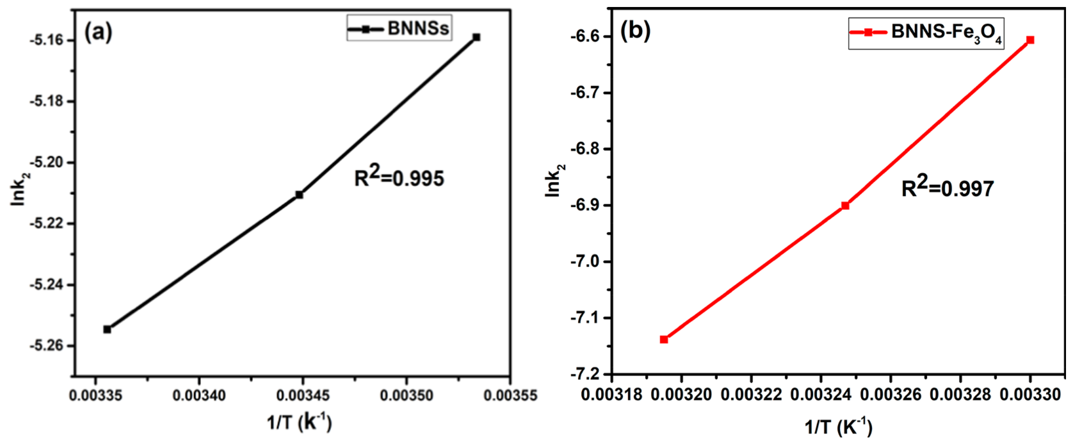

Figure 10. Linear form of Arrhenius equation for determination of activation energy: (a) BNNSs and (b) BNNS−Fe_3O_4 nanocomposite.

Table 3. As(V) Concentration after Adsorption on BNNS−Fe_3O_4 (Experimental Conditions: pH, 2.0; Dose of Adsorbent, 0.4 g L^{-1}; Temperature, 25 °C)

As(V) ion initial conc. before adsorption (ppb)	remaining As(V) ion conc. after adsorption (ppb)
535	4.08 ± 0.10
749	7.37 ± 0.25
856	9.18 ± 0.30

pH. Similar observations have been reported previously in the literature.[18,44,45,61] Further, As(V) ions were adsorbed on BNNS−FeOH through the ligand-exchange mechanism, in which there is replacement of hydroxyl ions by arsenate oxyanion. Moreover, As(V) ions form inner sphere complex.[44,62] At a low pH, bidentate formation is preferred and the sorption of arsenate on the surface of a BNNS−Fe_3O_4 may be through the following equations[63]

$$FeOH^{-1/2} + H^+_{aq} + AsO_4^-{}_{(aq)} \rightarrow FeOAsO_3 + H_2O \text{ (monodentate)} \quad (7)$$

$$2FeOH^{-1/2} + 2H^+_{aq} + AsO_4^-{}_{(aq)} \rightarrow Fe_2O_2AsO_3 + 2H_2O \text{ (bidentate)} \quad (8)$$

$$2FeOH^{-1/2} + 3H^+_{aq} + AsO_4^-{}_{(aq)} \rightarrow Fe_2O_2AsOOH_3 + 2H_2O \text{ (protonated bidentate)} \quad (9)$$

Hydroxyl groups (−OH) present on the surface of adsorbent are responsible for the adsorption of As(V) ions via chemisorption between arsenate oxyanion and the adsorbent.[38,64] Table 4 shows the As(V) ions' adsorption capacity reported by different adsorbents. The nanocomposite synthesized in this work shows better performance than most of the materials listed there.

3.5. Regeneration of BNNS−Fe_3O_4. Regeneration is the most important factor for the commercial application of an adsorbent. Figure 6a depicts that the adsorption capacity decreases with increase in pH. Therefore, the used adsorbent (BNNS−Fe_3O_4) was added into 1.0 M NaOH for 24 h.[65] To confirm the regeneration of the adsorbent, three samples were taken (named BNNS−Fe_3O_4 (pristine), BNNS−Fe_3O_4 (after adsorption), and BNNS−Fe_3O_4 (after desorption)) and characterized by FTIR spectroscopy (see Figure 11a). The FTIR spectra of BNNS−Fe_3O_4 (after adsorption) show a peak at ∼838.89 cm^{-1}, which represents As−O symmetric stretching vibration.[66] It confirmed that the As(V) ions were adsorbed on BNNS−Fe_3O_4 (pristine). The peak at ∼838.89 cm^{-1} was found to be absent after regeneration, which

Table 4. Comparison of Adsorption Capacities of Various Adsorbents

adsorbent	pH	conc./conc. range (ppm)	adsorption capacity (mg g^{-1})	separation	regeneration	references
cupric oxide nanoparticles	8.0	0.1−100	22.6	not reported	not reported	13
Fe_3O_4	4.0	10.63	4.65	not reported	not reported	14
kaolinite	5.0	10−200	0.86	not reported	not reported	15
magnetite-reduced graphene oxide composites	7.0	3−7	5.83	not reported	not reported	18
IAC−Fe(III)	3.0	0.5−8.5	3.00	not reported	not reported	9
Fe_{10}MCM-41silica	7.0		26.25	not reported	not reported	19
iron oxide multiwalled carbon nanotube hybrid	4.0		0.189	not reported	not reported	20
nano-zero-valent iron on activated carbon	6.5		12.0	not reported	reported	44
functionalized synthetic graphite	3.9−4.5	0.1−50	19.10	not reported	reported	67
porous iron oxide on activated carbon	7.0	5	27.78	not reported	not reported	68
Go/ferric hydroxide composite	4−7		23.78	not reported	not reported	69
ZMA (Sonora)	4.0	0.1−4	0.10	not reported	not reported	70
Fe−GO nanocomposite	4.0	5.0	3.26	reported	not reported	71
Fe_3O_4−RGO nanocomposite	7.0	1−10	16.0	reported	not reported	72
BNNS−Fe_3O_4 Nanocomposite	2.0	0.5−100	26.31	reported	reported	this study

DOI: 10.1021/acsami.8b22401
ACS Appl. Mater. Interfaces 2019, 11, 19017−19028

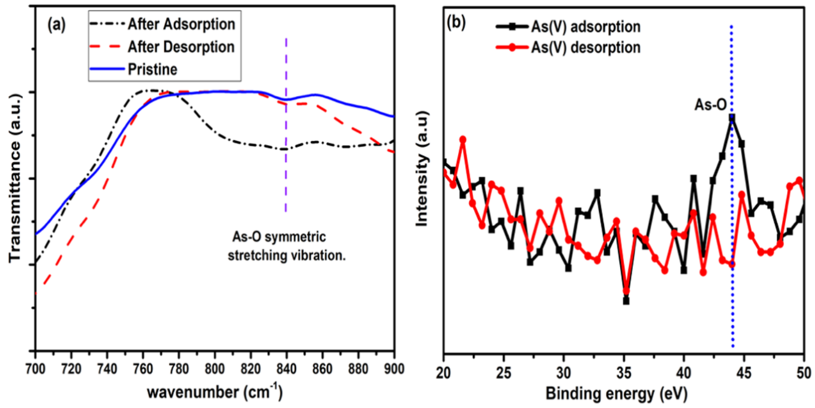

Figure 11. (a) FTIR and (b) XPS images of As(V) ions after adsorption and desorption on BNNS−Fe_3O_4 nanocomposite.

confirmed that the As(V) ions were removed from the BNNS−Fe_3O_4 (after adsorption) adsorbent. Furthermore, we have carried out XPS analysis of BNNS−Fe_3O_4 (after adsorption) and BNNS−Fe_3O_4 (after desorption). The XPS images of As(V) ions adsorption and desorption in Figure 11b clearly show that there is no As−O bonding at 43.92 eV after desorption in the desorbed material.[66] The FTIR and XPS results confirmed that the regenerated BNNS−Fe_3O_4 retained the same adsorption capacity. Therefore, the desorption method is quite effective.

4. CONCLUSIONS

In this work, BNNSs and BNNS−Fe_3O_4 nanocomposite adsorbents were synthesized and characterized to examine their potential for separation of As(V) ions from water. The SBET of the BNNSs and BNNS−Fe_3O_4 nanocomposite were found to be 1599.1 and 119.1 $m^2\ g^{-1}$, respectively. The pH study revealed that highest adsorption could be acquired at low pH (pH = 2) because of electrostatic attraction between positive charge on the adsorbent and oxyanions of As(V), which are negatively charged. Besides, it was observed that as the temperature increased, the adsorption capacity of BNNS−Fe_3O_4 also increased. It was found to be maximum at 30 °C. During adsorption of As(V) ions, the kinetics studies indicated that both the adsorbents followed the PSO kinetic model. The Langmuir model was followed by adsorption isotherms of both the adsorbents. The BNNS−Fe_3O_4 nanocomposite showed a significantly high maximum adsorption capacity (26.31 mg g^{-1}) of As(V) ions compared to the bare BNNSs adsorbent (5.30 mg g^{-1}) due to chemical adsorption. This 5-fold increase is in close agreement with the DFT calculations that were performed to calculate the binding energies of the two adsorbents. It is observed that the BNNS−Fe_3O_4 nanocomposite was capable of reducing up to 856 ppb of As(V) ions to below 10 ppb that is recommended by WHO for drinking purpose. The adsorbent could be easily separated from water due to its superparamagnetic nature at room temperature and also depicted regeneration behavior. Therefore, the synthesized BNNS−Fe_3O_4 nanocomposite depicts high potential for remediation of As(V) ions from contaminated water.

■ ASSOCIATED CONTENT

Supporting Information

The Supporting Information is available free of charge on the ACS Publications website at DOI: 10.1021/acsami.8b22401.

FESEM images, N_2 isotherm, pore size distribution, and XRD patterns of BNNSs and BNNS−Fe_3O_4 nanocomposite (PDF)

■ AUTHOR INFORMATION

Corresponding Author

*E-mail: nsinha@iitk.ac.in. Tel: (0512) 6797196. Fax: (0512) 6797408.

ORCID

Raghubeer S. Bangari: 0000-0001-6828-7456
Jayant K. Singh: 0000-0001-8056-2115
Niraj Sinha: 0000-0001-6600-9313

Notes

The authors declare no competing financial interest.

■ ACKNOWLEDGMENTS

This work was supported by Department of Science and Technology, Government of India, under Water Technology Initiative [project number DST/TM/WTI/2K15/112].

■ REFERENCES

(1) Su, H.; Ye, Z.; Hmidi, N. High-Performance Iron Oxide-Graphene Oxide Nanocomposite Adsorbents for Arsenic Removal. *Colloids Surf., A* **2017**, *522*, 161−172.
(2) Sinha, N. Nanomaterials-Based Solutions: Detection of Arsenic in Contaminated Water. *IEEE Nanotechnol. Mag.* **2014**, *8*, 17−23.
(3) Aragay, G.; Pons, J.; Merkoçi, A. Recent Trends in Macro-, Micro-, and Nanomaterial-Based Tools and Strategies for Heavy-Metal Detection. *Chem. Rev.* **2011**, *111*, 3433−3458.
(4) Guan, X.; Du, J.; Meng, X.; Sun, Y.; Sun, B.; Hu, Q. Application of Titanium Dioxide in Arsenic Removal from Water: A Review. *J. Hazard. Mater.* **2012**, *215−216*, 1−16.
(5) Chakraborti, D.; Rahman, M. M.; Ahamed, S.; Dutta, R. N.; Pati, S.; Mukherjee, S. C. Arsenic Groundwater Contamination and Its Health Effects in Patna District (Capital of Bihar) in the Middle Ganga Plain, India. *Chemosphere* **2016**, *152*, 520−529.
(6) Srivastava, S.; Sharma, Y. K. Arsenic Occurrence and Accumulation in Soil and Water of Eastern Districts of Uttar Pradesh, India. *Environ. Monit. Assess.* **2013**, *185*, 4995−5002.
(7) Nickson, R.; Sengupta, C.; Mitra, P.; Dave, S. N.; Banerjee, A. K.; Bhattacharya, A.; Basu, S.; Kakoti, N.; Moorthy, N. S.; Wasuja, M.; Kumar, M.; Mishra, D.; Ghosh, A.; Vaish, D. P.; Srivastava, A. K.; Tripathi, R. M.; Singh, S. N.; Prasad, R.; Bhattacharya, S.; Deverill, P. Current Knowledge on the Distribution of Arsenic in Groundwater in Five States of India. *J. Environ. Sci. Health, Part A: Toxic/Hazard. Subst. Environ. Eng.* **2007**, *42*, 1707−1718.

(8) Smedley, P. L.; Kinniburgh, D. G. A Review of the Source, Behaviour and Distribution of Arsenic in Natural Waters. *Appl. Geochem.* **2002**, *17*, 517−568.
(9) Tuna, A.Ö.A.; Özdemir, E.; Şimşek, E. B.; Beker, U. Removal of As(V) from Aqueous Solution by Activated Carbon-Based Hybrid Adsorbents: Impact of Experimental Conditions. *Chem. Eng. J.* **2013**, *223*, 116−128.
(10) Gómez-Pastora, J.; Bringas, E.; Ortiz, I. Recent Progress and Future Challenges on the Use of High Performance Magnetic Nano-Adsorbents in Environmental Applications. *Chem. Eng. J.* **2014**, *256*, 187−204.
(11) Kumar, S.; Nair, R. R.; Pillai, P. B.; Gupta, S. N.; Iyengar, M. A. R.; Sood, A. K. Graphene Oxide−MnFe2O4 Magnetic Nanohybrids for Efficient Removal of Lead and Arsenic from Water. *ACS Appl. Mater. Interfaces* **2014**, *6*, 17426−17436.
(12) Bang, S.; Patel, M.; Lippincott, L.; Meng, X. Removal of Arsenic from Groundwater by Granular Titanium Dioxide Adsorbent. *Chemosphere* **2005**, *60*, 389−397.
(13) Martinson, C. A.; Reddy, K. J. Adsorption of arsenic(III) and arsenic(V) by Cupric Oxide Nanoparticles. *J. Colloid Interface Sci.* **2009**, *336*, 406−411.
(14) Zhong, L. S.; Hu, J. S.; Liang, H. P.; Cao, A. M.; Song, W. G.; Wan, L. J. Self-Assembled 3D Flowerlike Iron Oxide Nanostructures and Their Application in Water Treatment. *Adv. Mater.* **2006**, *18*, 2426−2431.
(15) Mohapatra, D.; Mishra, D.; Chaudhury, G. R.; Das, R. P. Arsenic Adsorption Mechanism on Clay Minerals and Its Dependence on Temperature. *Korean J. Chem. Eng.* **2007**, *24*, 426−430.
(16) Mondal, P.; Balomajumder, C.; Mohanty, B. A Laboratory Study for the Treatment of Arsenic, Iron, and Manganese Bearing Ground Water Using Fe^{3+} Impregnated Activated Carbon: Effects of Shaking Time, pH and Temperature. *J. Hazard. Mater.* **2007**, *144*, 420−426.
(17) Di Natale, F.; Erto, A.; Lancia, A.; Musmarra, D. Experimental and Modelling Analysis of As(V) Ions Adsorption on Granular Activated Carbon. *Water Res.* **2008**, *42*, 2007−2016.
(18) Chandra, V.; Park, J.; Chun, Y.; Lee, J. W.; Hwang, I. C.; Kim, K. S. Water-Dispersible Magnetite-Reduced Graphene Oxide Composites for Arsenic Removal. *ACS Nano* **2010**, *4*, 3979−3986.
(19) Li, F. Layer-by-Layer Loading Iron onto Mesoporous Silica Surfaces: Synthesis, Characterization and Application for As(V) Removal. *Microporous Mesoporous Mater.* **2013**, *171*, 139−146.
(20) Addo Ntim, S.; Mitra, S. Removal of Trace Arsenic to Meet Drinking Water Standards Using Iron Oxide Coated Multiwall Carbon Nanotubes. *J. Chem. Eng. Data* **2011**, *56*, 2077−2083.
(21) Zong, P.; Wang, S.; Zhao, Y.; Wang, H.; Pan, H.; He, C. Synthesis and Application of Magnetic Graphene/iron Oxides Composite for the Removal of U(VI) from Aqueous Solutions. *Chem. Eng. J.* **2013**, *220*, 45−52.
(22) Zong, P.; Cao, D.; Cheng, Y.; Wang, S.; Hayat, T.; Alharbi, N. S.; Guo, Z.; Zhao, Y.; He, C. Enhanced Performance for Eu(iii) Ion Remediation Using Magnetic Multiwalled Carbon Nanotubes Functionalized with Carboxymethyl Cellulose Nanoparticles Synthesized by Plasma Technology. *Inorg. Chem. Front.* **2018**, *5*, 3184−3196.
(23) Li, L. H.; Cervenka, J.; Watanabe, K.; Taniguchi, T.; Chen, Y. Strong Oxidation Resistance of Atomically Thin Boron Nitride Nanosheets. *ACS Nano* **2014**, *8*, 1457−1462.
(24) Lei, W.; Portehault, D.; Liu, D.; Qin, S.; Chen, Y. Porous Boron Nitride Nanosheets for Effective Water Cleaning. *Nat. Commun.* **2013**, *4*, No. 1777.
(25) Li, J.; Lin, J.; Xu, X.; Zhang, X.; Xue, Y.; Mi, J.; Mo, Z.; Fan, Y.; Hu, L.; Yang, X.; Zhang, J.; Meng, F.; Yuan, S.; Tang, C. Porous Boron Nitride with a High Surface Area: Hydrogen Storage and Water Treatment. *Nanotechnology* **2013**, *24*, No. 155603.
(26) Yanai, T.; Tew, D. P.; Handy, N. C. A New Hybrid Exchange-Correlation Functional Using the Coulomb-Attenuating Method (CAM-B3LYP). *Chem. Phys. Lett.* **2004**, *393*, 51−57.
(27) Nag, A.; Raidongia, K.; Hembram, K. P. S. S.; Datta, R.; Waghmare, U. V.; Rao, C. N. R. Graphene Analogues of BN: Novel Synthesis and Properties. *ACS Nano* **2010**, *4*, 1539−1544.
(28) Kumari, M.; Pittman, C. U.; Mohan, D. Heavy Metals [Chromium (VI) and Lead (II)] Removal from Water Using Mesoporous Magnetite (Fe_3O_4) Nanospheres. *J. Colloid Interface Sci.* **2015**, *442*, 120−132.
(29) Chen, R.; Zhi, C.; Yang, H.; Bando, Y.; Zhang, Z.; Sugiur, N.; Golberg, D. Arsenic (V) Adsorption on Fe_3O_4 Nanoparticle-Coated Boron Nitride Nanotubes. *J. Colloid Interface Sci.* **2011**, *359*, 261−268.
(30) Yang, Y.; Chun, Y.; Shang, G.; Huang, M. pH-Dependence of Pesticide Adsorption by Wheat-Residue-Derived Black Carbon. *Langmuir* **2004**, *20*, 6736−6741.
(31) Andersson, K. I.; Eriksson, M.; Norgren, M. Removal of Lignin from Wastewater Generated by Mechanical Pulping Using Activated Charcoal and Fly Ash: Adsorption Isotherms and Thermodynamics. *Ind. Eng. Chem. Res.* **2011**, *50*, 7722−7732.
(32) Anota, E. C.; Villanueva, M. S.; Morales, A. E.; Castro, M. Stability, Electronic and Magnetic Properties of the Octagraphene-like Boron Nitride Nanosheets: In Silico Studies. *Fullerenes, Nanotubes, Carbon Nanostruct.* **2018**, *26*, 93−99.
(33) Xue, L.; Lu, B.; Wu, Z.-S.; Ge, C.; Wang, P.; Zhang, R.; Zhang, X.-D. Synthesis of Mesoporous Hexagonal Boron Nitride Fibers with High Surface Area for Efficient Removal of Organic Pollutants. *Chem. Eng. J.* **2014**, *243*, 494−499.
(34) Mou, Y.; Yang, H.; Xu, Z. Morphology, Surface Layer Evolution, and Structure-Dye Adsorption Relationship of Porous Fe3O4MNPs Prepared by Solvothermal/Gas Generation Process. *ACS Sustainable Chem. Eng.* **2017**, *5*, 2339−2349.
(35) Banerjee, S. S.; Chen, D.-H. Fast Removal of Copper Ions by Gum Arabic Modified Magnetic Nano-Adsorbent. *J. Hazard. Mater.* **2007**, *147*, 792−799.
(36) Zhuang, L.; Zhang, W.; Zhao, Y.; Shen, H.; Lin, H.; Liang, J. Preparation and Characterization of Fe3O4 Particles with Novel Nanosheets Morphology and Magnetochromatic Property by a Modified Solvothermal Method. *Sci. Rep.* **2015**, *5*, No. 9320.
(37) Xia, H. B.; Foo, P.; Yi, J. Water-Dispersible Spherically Hollow Clusters of Magnetic Nanoparticles. *Chem. Mater.* **2009**, *21*, 2442−2451.
(38) Du, Y.; Fan, H.; Wang, L.; Wang, J.; Wu, J.; Dai, H. α-Fe_2O_3 Nanowires Deposited Diatomite: Highly Efficient Absorbents for the Removal of Arsenic. *J. Mater. Chem. A* **2013**, *1*, 7729.
(39) Lunge, S.; Singh, S.; Sinha, A. Magnetic Iron Oxide (Fe_3O_4) Nanoparticles from Tea Waste for Arsenic Removal. *J. Magn. Magn. Mater.* **2014**, 21−31.
(40) Liu, F.; Yu, J.; Ji, X.; Qian, M. Nanosheet-Structured Boron Nitride Spheres with a Versatile Adsorption Capacity for Water Cleaning. *ACS Appl. Mater. Interfaces* **2015**, *7*, 1824−1832.
(41) Li, J.; Xiao, X.; Xu, X.; Lin, J.; Huang, Y.; Xue, Y.; Jin, P.; Zou, J.; Tang, C. Activated Boron Nitride as an Effective Adsorbent for Metal Ions and Organic Pollutants. *Sci. Rep.* **2013**, *3*, No. 3208.
(42) Singh, K. P.; Singh, A. K.; Gupta, S.; Rai, P. Modeling and Optimization of Reductive Degradation of Chloramphenicol in Aqueous Solution by Zero-Valent Bimetallic Nanoparticles. *Environ. Sci. Pollut. Res.* **2012**, *19*, 2063−2078.
(43) Mohan, D.; Pittman, C. U. Arsenic Removal from Water/wastewater Using adsorbents—A Critical Review. *J. Hazard. Mater.* **2007**, *142*, 1−53.
(44) Zhu, H.; Jia, Y.; Wu, X.; Wang, H. Removal of Arsenic from Water by Supported Nano Zero-Valent Iron on Activated Carbon. *J. Hazard. Mater.* **2009**, *172*, 1591−1596.
(45) Guo, X.; Chen, F. Removal of Arsenic by Bead Cellulose Loaded with Iron Oxyhydroxide from Groundwater. *Environ. Sci. Technol.* **2005**, *39*, 6808−6818.
(46) Yang, K.; Chen, B.; Zhu, L. Graphene-Coated Materials Using Silica Particles as a Framework for Highly Efficient Removal of Aromatic Pollutants in Water. *Sci. Rep.* **2015**, *5*, No. 11641.

(47) Zhao, J.; Wang, Z.; Zhao, Q.; Xing, B. Adsorption of Phenanthrene on Multilayer Graphene as Affected by Surfactant and Exfoliation. *Environ. Sci. Technol.* **2014**, *48*, 331−339.
(48) Thomas, J. M. The Existence of Endothermic Adsorption. *J. Chem. Educ.* **1961**, *38*, No. 138.
(49) Asfour, H. M.; Fadali, O. A.; Nassar, M. M.; El-Geundi, M. S. Equilibrium Studies on Adsorption of Basic Dyes on Hardwood. *J. Chem. Technol. Biotechnol., Chem. Technol.* **1985**, *35*, 21−27.
(50) Mahmoodi, N. M.; Hayati, B.; Arami, M.; Lan, C. Adsorption of Textile Dyes on Pine Cone from Colored Wastewater: Kinetic, Equilibrium and Thermodynamic Studies. *Desalination* **2011**, *268*, 117−125.
(51) Boyd, G. E.; Adamson, A. W.; Myers, L. S. The Exchange Adsorption of Ions from Aqueous Solutions by Organic Zeolites. II. Kinetics1. *J. Am. Chem. Soc.* **1947**, *69* (11), 2836−2848.
(52) Saha, P.; Chowdhury, S. Insight Into Adsorption Thermodynamics. In *Thermodynamics*; Tadashi, P. M., Ed.; InTech, 2011; pp 349−364.
(53) Pokhrel, D.; Viraraghavan, T. Arsenic Removal from an Aqueous Solution by Modified A. Niger Biomass: Batch Kinetic and Isotherm Studies. *J. Hazard. Mater.* **2008**, *150*, 818−825.
(54) Li, H.; Huang, G.; An, C.; Hu, J.; Yang, S. Removal of Tannin from Aqueous Solution by Adsorption onto Treated Coal Fly Ash: Kinetic, Equilibrium, and Thermodynamic Studies. *Ind. Eng. Chem. Res.* **2013**, *52*, 15923−15931.
(55) Unuabonah, E. I.; Adebowale, K. O.; Olu-Owolabi, B. I. Kinetic and Thermodynamic Studies of the Adsorption of Lead (II) Ions onto Phosphate-Modified Kaolinite Clay. *J. Hazard. Mater.* **2007**, *144*, 386−395.
(56) Peter, R.; Hugh, B.; Keith, R. *Arsenic Pollution: A Global Synthesis*; Wiley-Blackwell, 2009.
(57) Ferguson, J. F.; Gavis, J. A Review of the Arsenic Cycle in Natural Waters. *Water Res.* **1972**, *6*, 1259−1274.
(58) Smedley, P.; Kinniburgh, D. A Review of the Source, Behaviour and Distribution of Arsenic in Natural Waters. *Appl. Geochem.* **2002**, *17*, 517−568.
(59) Chen, M.; Shafer-Peltier, K.; Randtke, S. J.; Peltier, E. Modeling Arsenic (V) Removal from Water by Micellar Enhanced Ultrafiltration in the Presence of Competing Anions. *Chemosphere* **2018**, *213*, 285−294.
(60) Welch, A. H.; Westjohn, D. B.; Helsel, D. R.; Wanty, R. B. Arsenic in Ground Water of the United States: Occurrence and Geochemistry. *Ground Water* **2000**, *38*, 589−604.
(61) La, D. D.; Patwari, J. M.; Jones, L. A.; Antolasic, F.; Bhosale, S. V. Fabrication of a GNP/Fe-Mg Binary Oxide Composite for Effective Removal of Arsenic from Aqueous Solution. *ACS Omega* **2017**, *2*, 218−226.
(62) Vaughan, R. L.; Reed, B. E. Modeling As(V) Removal by a Iron Oxide Impregnated Activated Carbon Using the Surface Complexation Approach. *Water Res.* **2005**, *39*, 1005−1014.
(63) Hiemstra, T.; van Riemsdijk, W. H. Surface Structural Ion Adsorption Modeling of Competitive Binding of Oxyanions by Metal (Hydr)oxides. *J. Colloid Interface Sci.* **1999**, *210*, 182−193.
(64) Hristovski, K. D.; Westerhoff, P. K.; Crittenden, J. C.; Olson, L. W. Arsenate Removal by Nanostructured ZrO2 Spheres. *Environ. Sci. Technol.* **2008**, *42*, 3786−3790.
(65) Yoon, Y.; Zheng, M.; Ahn, Y. T.; Park, W. K.; Yang, W. S.; Kang, J. W. Synthesis of Magnetite/non-Oxidative Graphene Composites and Their Application for Arsenic Removal. *Sep. Purif. Technol.* **2017**, *178*, 40−48.
(66) Penke, Y. K.; Anantharaman, G.; et al. Aluminum Substituted Nickel Ferrite (Ni−Al−Fe): A Ternary Metal Oxide Adsorbent for Arsenic Adsorption in Aqueous Medium. *RSC Adv.* **2016**, *6*, 55608−55617.
(67) Uppal, H.; Hemlata; Tawale, J.; Singh, N. Zinc Peroxide Functionalized Synthetic Graphite: An Economical and Efficient Adsorbent for Adsorption of Arsenic (III) and (V). *J. Environ. Chem. Eng.* **2016**, *4*, 2964−2975.
(68) Yürüm, A.; Kocabaş-Atakli, Z. Ö.; Sezen, M.; Semiat, R.; Yürüm, Y. Fast Deposition of Porous Iron Oxide on Activated Carbon by Microwave Heating and Arsenic (V) Removal from Water. *Chem. Eng. J.* **2014**, *242*, 321−332.
(69) Zhang, K.; Dwivedi, V.; Chi, C.; Wu, J. Graphene Oxide/ferric Hydroxide Composites for Efficient Arsenate Removal from Drinking Water. *J. Hazard. Mater.* **2010**, *182*, 162−168.
(70) Elizalde-González, M. P.; Mattusch, J.; Wennrich, R.; Morgenstern, P. Uptake of Arsenite and Arsenate by Clinoptilote-Rich Tuffs. *Microporous Mesoporous Mater.* **2001**, *46*, 277−286.
(71) Gollavelli, G.; Chang, C. C.; Ling, Y. C. Facile Synthesis of Smart Magnetic Graphene for Safe Drinking Water: Heavy Metal Removal and Disinfection Control. *ACS Sustainable Chem. Eng.* **2013**, *1*, 462−472.
(72) Paul, B.; Parashar, V.; Mishra, A. Graphene in the Fe3O4 Nano-Composite Switching the Negative Influence of Humic Acid Coating into an Enhancing Effect in the Removal of Arsenic from Water. *Environ. Sci.: Water Res. Technol.* **2015**, *1*, 77−83.

DOI: 10.1021/acsami.8b22401
ACS Appl. Mater. Interfaces 2019, 11, 19017−19028